

# Theory and numerics of geometrically non-linear open system mechanics

E. Kuhl and P. Steinmann<sup>\*,†</sup>

*Lehrstuhl für Technische Mechanik, Universität Kaiserslautern, Kaiserslautern D-67653, Germany*

## SUMMARY

The present contribution aims at deriving a general theoretical and numerical framework for open system thermodynamics. The balance equations for open systems differ from the classical balance equations by additional terms arising from possible local changes in mass. In contrast to existing formulations, these changes not only originate from additional mass sources or sinks but also from a possible in- or outflux of matter. Constitutive equations for the mass source and the mass flux are discussed for the particular model problem of bone remodelling in hard tissue mechanics. Particular emphasis is dedicated to the spatial discretization of the coupled system of the balance of mass and momentum. To this end we suggest a geometrically non-linear monolithic finite element based solution technique introducing the density and the deformation map as primary unknowns. It is supplemented by the consistent linearization of the governing equations. The resulting algorithm is validated qualitatively for classical examples from structural mechanics as well as for biomechanical applications with particular focus on the functional adaption of bones. It turns out that, owing to the additional incorporation of the mass flux, the proposed model is able to simulate size effects typically encountered in microstructural materials such as open-pored cellular solids, e.g. bones. Copyright © 2003 John Wiley & Sons, Ltd.

KEY WORDS: finite element method; open systems; thermodynamics; biomechanics; functional adaption of bones

## 1. INTRODUCTION

In traditional non-relativistic closed-system mechanics, the amount of matter contained in a given reference body is typically considered a conservation property which does not change, no matter how the body is displaced, deformed or accelerated. Nevertheless, this conservation of mass, which is nothing but a mere definition, can no longer be considered a reasonable assumption in modern bio- or chemomechanical applications. Herein, changes in mass can either be caused by the local absorption or resorption of mass or by a possible in- or

---

\*Correspondence to: P. Steinmann, Lehrstuhl für Technische Mechanik, Universität Kaiserslautern, Kaiserslautern D-67653, Germany.

†E-mail: ps@rhrk.uni-kl.de

Contract/grant sponsor: German Science Foundation DFG; contract/grant number: KU-1313

*Received 1 August 2002*

*Revised 2 December 2002*

*Accepted 27 January 2003*

outflux of matter. In biomechanics, the former is typically related to proliferation, hyperplasia, hypertrophy or atrophy while the latter is motivated by the migration or movement of cells, see e.g. References [1–4]. Leaching of chemical reactants or the motion of a burning body typically encountered in rocket propulsion furnish classical examples of open systems in chemomechanical applications, see e.g. Reference [5, Section 1.6]; [6, Section 1.4.6] or [7, Section 3.5]. Maugin [8] visualized open systems as being enclosed by a permeable, deformable and diathermal membrane through which the open system is allowed to exchange mass, momentum, energy and entropy with the ‘outside world’. As opposed to the theory of open systems, the ‘theory of mixtures’ incorporates the influence of the outside world in the form of additional constituents obeying their own individual balance laws. In this context, the constituents are allowed to exchange mass, momentum, energy and entropy amongst themselves while the mass of the overall mixture remains constant, see e.g. References [14, 15, 35].

In the case of open system mechanics, however, attention is confined to one constituent alone, which, in our case, dominates the overall mechanical behaviour, such as the bone matrix in hard tissue mechanics. The first theory of open system mechanics has been presented more than a quarter of a century ago by Cowin and Hegedus [12] under the name of ‘theory of adaptive elasticity’. Herein, the influence of the outside world has a priori been restricted to volume source terms. Just recently, this basic theory has been enhanced to yield the ‘theory of volumetric growth’ by Epstein and Maugin [13] who allow for additional surface flux exchanges. Herein, we will apply an alternative introduction of the flux terms as demonstrated in our own recent works [14, 15, 35].

Since the beginning of the 1990s, the ‘theory of adaptive elasticity’ gained an enormous attention in the community of biomechanics where it is usually referred to as ‘theory of functional adaptation’. The governing equations could finally be solved numerically with the help of the finite element method, see e.g. References [16–24] or the recent textbook of Carter and Beaupré [25]. The resulting algorithm was even applied to predict the remodelling of bone around implants, see Reference [26] or [27]. However, most formulations based on a staggered solution of the balance of mass, the so-called ‘biological equilibrium’ and the balance of momentum, the ‘mechanical equilibrium’, yield unstable or non-physical results, see e.g. Reference [17]. This presentation aims at deriving a monolithic solution strategy with the material density and the deformation as primary unknowns. The resulting two-field finite element formulation naturally lends itself to a stable and robust algorithm for open system mechanics. While the focus of the present contribution is basically dedicated to the derivation of one particular monolithic solution strategy, different discretization techniques are compared in our current research work, see Reference [28]. In contrast to the existing formulations in the literature, we shall allow for an additional possible in- or outflux of mass. It turns out, that the resulting algorithm is able to capture size effects in a natural and physically motivated way.

This manuscript is organized as follows. Section 2 briefly reiterates the fundamental balance equations of open system thermodynamics. The resulting dissipation inequality places further restrictions on the choice of constitutive response functions which is illustrated in Section 3 for the particular case of hard biological tissues. In Section 4, we derive the finite element formulation of the coupled problem by introducing the material density and the deformation map as nodal degrees of freedom. A monolithic solution strategy supplemented by the consistent linearization of the balance of mass and momentum is proposed. The study of the sensitivity towards the choice of the constitutive parameters is the subject of Section 5, where we

analyse selected one-dimensional prototype examples. Section 6 illustrates the functionality of the suggested algorithm with the help of classical examples taken from topology optimization. Next, the derived algorithm is applied to typical examples of bone remodelling in Section 7. Final conclusions are drawn in Section 8.

## 2. BALANCE EQUATIONS FOR OPEN SYSTEMS

To set the stage, we briefly reiterate the kinematics of geometrically non-linear continuum mechanics. The kinematic description is primarily characterized through the deformation map  $\varphi$  mapping the material placement  $\mathbf{X}$  of a physical particle in the material configuration  $\mathcal{B}_0$  to its spatial placement  $\mathbf{x}$  in the spatial configuration  $\mathcal{B}_t$  as  $\mathbf{x} = \varphi(\mathbf{X}, t): \mathcal{B}_0 \rightarrow \mathcal{B}_t$ . The related deformation gradient  $\mathbf{F} = \nabla\varphi(\mathbf{X}, t): T\mathcal{B}_0 \rightarrow T\mathcal{B}_t$  and its Jacobian  $J = \det \mathbf{F} > 0$  define the linear tangent map from the material tangent space  $T\mathcal{B}_0$  to the spatial tangent space  $T\mathcal{B}_t$ . Typically, the right and left Cauchy–Green strain tensors  $\mathbf{C} = \mathbf{F}^t \cdot \mathbf{F}$  and  $\mathbf{b} = \mathbf{F} \cdot \mathbf{F}^t$  or their inverses  $\mathbf{B} = \mathbf{C}^{-1}$  and  $\mathbf{c} = \mathbf{b}^{-1}$  are introduced as a characteristic strain measures. Let  $D_t = \partial_t \{\cdot\}|_X$  denote the material time derivative of a quantity  $\{\cdot\}$  at fixed material placement  $\mathbf{X}$ . The spatial velocity  $\mathbf{v} = D_t\varphi(\mathbf{X}, t)$  can thus be understood as the material time derivative of the deformation map  $\varphi$ . Note, that its material gradient  $\nabla\mathbf{v}$  is identical to the material time derivative of the deformation gradient  $\mathbf{F}$  as  $D_t\mathbf{F} = \nabla\mathbf{v}$ . Throughout the entire analysis, we shall apply a formulation with material reference. Thus,  $\nabla\{\cdot\}$  and  $\text{Div}\{\cdot\}$  denote the gradient and the divergence of the field  $\{\cdot\}$  with respect to the material placement  $\mathbf{X}$ . In what follows, we shall strictly distinguish between volume specific scalar-valued or tensorial quantities with material reference  $\{\cdot\}_0$  and the corresponding mass specific quantities  $\{\cdot\}$ , whereby both are related through the material density  $\rho_0$  as  $\{\cdot\}_0 = \rho_0\{\cdot\}$ . With the above definitions at hand, we will now introduce the balance equations for open systems. Hereby, we basically follow the approach suggested by Kuhl and Steinmann [14, 15]. By assuming that sufficient smoothness criteria are fulfilled by the related fields, we can restrict ourselves to the local or rather differential form of the balance laws rather than considering their global or integral format.

### 2.1. Balance of mass

While in classical closed system mechanics, the amount of matter contained in a body  $\mathcal{B}_0$  generally does not change, the mass of a reference body can no longer be considered a conservation property within the thermodynamics of open systems. Taking into account this basic feature of open systems, the balance of mass states that the rate of change of the material density  $\rho_0$  be in equilibrium with the influx of mass  $\mathbf{R}$  and the amount of locally created mass  $\mathcal{R}_0$ .

$$D_t\rho_0 = \text{Div} \mathbf{R} + \mathcal{R}_0 \tag{1}$$

The balance of mass plays a crucial role in the present theory since it can be used to transform any other volume specific balance law in its mass specific counterpart.

### 2.2. Balance of momentum

The volume specific balance of linear momentum balances the rate of change of the volume specific momentum density  $\mathbf{p}_0 = \rho_0\mathbf{p}$  with the momentum flux  $\bar{\mathbf{I}}^t + \mathbf{p} \otimes \mathbf{R}$  and the momentum

source  $\bar{\mathbf{b}}_0 + \mathbf{p}\mathcal{R}_0 - \nabla\mathbf{p} \cdot \mathbf{R}$  whereby  $\mathbf{p}$  is nothing but the spatial velocity as  $\mathbf{p} = D_t\boldsymbol{\varphi}(\mathbf{X}, t) = \mathbf{v}$ .

$$D_t\mathbf{p}_0 = \text{Div}(\bar{\boldsymbol{\Pi}}^t + \mathbf{p} \otimes \mathbf{R}) + \bar{\mathbf{b}}_0 + \mathbf{p}\mathcal{R}_0 - \nabla\mathbf{p} \cdot \mathbf{R} \tag{2}$$

Thereby, the total momentum flux consists of the reduced momentum flux  $\bar{\boldsymbol{\Pi}}^t$  and an additional flux contribution  $\mathbf{p} \otimes \mathbf{R}$  due to the newly in-flowing amount of matter  $\mathbf{R}$ . Equivalently, the momentum source consists of a reduced momentum source  $\bar{\mathbf{b}}_0$  enhanced by changes in momentum caused by the added mass  $\mathbf{p}\mathcal{R}_0 - \nabla\mathbf{p} \cdot \mathbf{R}$ . By subtracting  $\mathbf{p}$  times the balance of mass (1),

$$\mathbf{p}D_t\rho_0 = \text{Div}(\mathbf{p} \otimes \mathbf{R}) + \mathbf{p}\mathcal{R}_0 - \nabla\mathbf{p} \cdot \mathbf{R} \tag{3}$$

the volume specific balance of momentum (2) can be transformed into its mass specific counterpart.

$$\rho_0 D_t\mathbf{p} = \text{Div}\bar{\boldsymbol{\Pi}}^t + \bar{\mathbf{b}}_0 \tag{4}$$

On the Neumann boundary, the reduced momentum flux  $\bar{\boldsymbol{\Pi}}^t$  can be related to the closed and open system stress vector contributions  $\mathbf{t}^{\text{closed}}$  and  $\bar{\mathbf{t}}^{\text{open}}$  while the reduced momentum source  $\bar{\mathbf{b}}_0$  can be expressed as the sum of the classical volume force  $\mathbf{b}_0^{\text{closed}}$  and the reduced open system term  $\bar{\mathbf{b}}_0^{\text{open}}$ .

$$\bar{\boldsymbol{\Pi}}^t \cdot \mathbf{N} := \mathbf{t}^{\text{closed}} + \bar{\mathbf{t}}^{\text{open}}, \quad \bar{\mathbf{b}}_0 := \mathbf{b}_0^{\text{closed}} + \bar{\mathbf{b}}_0^{\text{open}} \tag{5}$$

### 2.3. Balance of internal energy

The volume specific version of the balance of internal energy governs the evolution of the volume specific internal energy density  $I_0 = \rho_0 I$ . Its rate of change is balanced with the internal mechanical power  $\bar{\mathbf{p}}_0^{\text{int}} = \bar{\boldsymbol{\Pi}}^t : D_t\mathbf{F}$  and the flux of non-mechanical energy which consists of the classical closed system contribution  $-\bar{\mathbf{Q}}$  and the additional term  $I\mathbf{R}$  accounting for the internal energy of the in-flowing mass. Moreover, we have to take into account the classical non-mechanical source term  $\bar{\mathcal{Q}}_0$  enhanced by the source terms  $I\mathcal{R}_0$  and  $-\nabla I \cdot \mathbf{R}$  due to internal energy changes caused by the added mass.

$$D_t I_0 = \text{Div}(-\bar{\mathbf{Q}} + I\mathbf{R}) + \bar{\mathcal{Q}}_0 + I\mathcal{R}_0 - \nabla I \cdot \mathbf{R} + \bar{\mathbf{p}}_0^{\text{int}} \tag{6}$$

A subtraction of the balance of mass (1) weighted by the internal energy  $I$

$$I D_t\rho_0 = \text{Div}(I\mathbf{R}) + I\mathcal{R}_0 - \nabla I \cdot \mathbf{R} \tag{7}$$

renders the mass specific version of the balance of internal energy.

$$\rho_0 D_t I = -\text{Div}\bar{\mathbf{Q}} + \bar{\mathcal{Q}}_0 + \bar{\mathbf{p}}_0^{\text{int}} \tag{8}$$

Similar to the reduced momentum flux, the reduced non-mechanical energy flux  $\bar{\mathbf{Q}}$  can be related to the closed and open system contributions  $q^{\text{closed}}$  and  $\bar{q}^{\text{open}}$  on the Neumann boundary. Moreover, the non-mechanical energy source  $\bar{\mathcal{Q}}_0$  can be expressed in terms of the classical closed system heat source  $\mathcal{Q}_0^{\text{closed}}$  and the additional open system contribution  $\bar{\mathcal{Q}}_0^{\text{open}}$ .

$$\bar{\mathbf{Q}} \cdot \mathbf{N} := q^{\text{closed}} + \bar{q}^{\text{open}}, \quad \bar{\mathcal{Q}}_0 := \mathcal{Q}_0^{\text{closed}} + \bar{\mathcal{Q}}_0^{\text{open}} \tag{9}$$

#### 2.4. Balance of entropy

Last, we introduce the balance of entropy for open systems. Its volume specific version balances the time rate of change of the volume specific entropy density  $S_0 = \rho_0 S$  with the entropy flux, the entropy source and the internal entropy production  $\bar{h}_0^{\text{int}}$ , whereby the latter is required to be non-negative throughout the entire thermodynamical process as  $\bar{h}_0^{\text{int}} \geq 0$ .

$$D_t S_0 = \text{Div}(-\bar{\mathbf{H}} + S\mathbf{R}) + \bar{\mathcal{H}}_0 + S\mathcal{R}_0 - \nabla S \cdot \mathbf{R} + \bar{h}_0^{\text{int}} \quad (10)$$

Herein, the entropy flux consists of the reduced entropy flux  $\bar{\mathbf{H}}$  enhanced by the amount of entropy carried by the in-flowing mass  $S\mathbf{R}$ . The entropy source is given as the sum of the reduced entropy source  $\bar{\mathcal{H}}_0$  and the additional open system contributions  $S\mathcal{R}_0$  and  $-\nabla S \cdot \mathbf{R}$ . Again, the corresponding mass specific version can be derived by subtracting a weighted version of the balance of mass (1)

$$SD_t \rho_0 = \text{Div}(S\mathbf{R}) + S\mathcal{R}_0 - \nabla S \cdot \mathbf{R} \quad (11)$$

from the volume specific balance of entropy (10).

$$\rho_0 D_t S = -\text{Div} \bar{\mathbf{H}} + \bar{\mathcal{H}}_0 + \bar{h}_0^{\text{int}} \quad (12)$$

The reduced flux and source term  $\bar{\mathbf{H}}$  and  $\bar{\mathcal{H}}_0$  of the mass specific version can be related to the sum of the corresponding classical closed system contributions  $h^{\text{closed}}$  and  $\mathcal{H}_0^{\text{closed}}$  and the open system terms  $\bar{h}^{\text{open}}$  and  $\bar{\mathcal{H}}_0^{\text{open}}$ .

$$\bar{\mathbf{H}} \cdot \mathbf{N} := h^{\text{closed}} + \bar{h}^{\text{open}}, \quad \bar{\mathcal{H}}_0 := \mathcal{H}_0^{\text{closed}} + \bar{\mathcal{H}}_0^{\text{open}} \quad (13)$$

For further elaborations, it proves elementary to set up relations between the reduced entropy flux  $\bar{\mathbf{H}}$  and the reduced non-mechanical energy flux  $\bar{\mathbf{Q}}$  as well as between the reduced entropy source  $\bar{\mathcal{H}}_0$  and the reduced non-mechanical energy source  $\bar{\mathcal{Q}}_0$  in terms of the absolute temperature  $\theta$ , an extra entropy flux  $\mathbf{S}$  and an extra entropy source  $\mathcal{S}_0$  as  $\bar{\mathbf{H}} = \bar{\mathbf{Q}}/\theta + \mathbf{S}$  and  $\bar{\mathcal{H}}_0 = \bar{\mathcal{Q}}_0/\theta + \mathcal{S}_0$ . The mass specific balance of entropy (12) can now be cast into the more familiar statement of the dissipation inequality by introducing the dissipation rate  $\bar{d}_0$  as the internal entropy production  $\bar{h}_0^{\text{int}}$  weighted by the absolute temperature  $\theta$ , thus  $\bar{d}_0 := \theta \bar{h}_0^{\text{int}} \geq 0$ . With the help of the mass specific balance of entropy (12) and the balance of internal energy (8) and the Legendre–Fenchel transform introducing the Helmholtz free energy as  $\Psi = I - \theta S$ , we obtain the Clausius–Duhem inequality for open system thermodynamics.

$$\bar{d}_0 = \bar{\mathbf{T}}^t : D_t \mathbf{F} - \rho_0 D_t \Psi - \rho_0 S D_t \theta + [\text{Div} \mathbf{S} - \mathcal{S}_0] \theta - \bar{\mathbf{Q}} \cdot \nabla \ln \theta \geq 0 \quad (14)$$

Herein, the non-standard term  $[\text{Div} \mathbf{S} - \mathcal{S}_0]$  accounts for the explicit exchanges of entropy with the outside world. The appropriate evaluation of the Clausius–Duhem inequality (14) and its impact on the choice of constitutive equations will be demonstrated in the following section.

##### Remark 2.1

As opposed to some former formulations in the literature, e.g. Reference [13], all our mass specific balance equations are free from any explicit open system contribution. In the mass specific format, the nature of the open system manifests itself only implicitly through the

boundary conditions, see also References [14, 15]. In what follows, we shall therefore exclusively elaborate the mass specific versions of the balance equations since they take the familiar format known from classical closed system thermodynamics.

### 3. CONSTITUTIVE EQUATIONS

In the present section, we shall introduce the constitutive equations based on the evaluation of the dissipation inequality derived in the previous section. For the sake of transparency, we shall restrict ourselves to the isothermal case in the sequel. Consequently, the volume specific free energy function  $\Psi_0 = \rho_0 \Psi$  can be expressed as a function of the local density  $\rho_0$  depending on the material placement  $\mathbf{X}$  and the time  $t$  and the mass specific free energy density  $\Psi$  which in turn can depend on the material density  $\rho_0$  and the deformation gradient  $\mathbf{F}$  with a possible explicit dependence on the material placement  $\mathbf{X}$ .

$$\Psi = \Psi(\rho_0, \mathbf{F}; \mathbf{X}), \quad \rho_0 = \rho_0(\mathbf{X}, t) \quad (15)$$

Consequently, the material time derivative of the mass specific free energy density is formally given in the following form.

$$D_t \Psi = D_{\rho_0} \Psi D_t \rho_0 + D_{\mathbf{F}} \Psi : D_t \mathbf{F} \quad (16)$$

The evaluation of the isothermal version of the Clausius–Duhem inequality, the so-called Clausius–Planck inequality,

$$\bar{d}_0 = -\rho_0 D_{\rho_0} \Psi D_t \rho_0 + [\bar{\mathbf{I}}^t - \rho_0 D_{\mathbf{F}} \Psi] : D_t \mathbf{F} + [\text{Div } \mathbf{S} - \mathcal{S}_0] \theta \geq 0 \quad (17)$$

yields the definition of the reduced momentum flux  $\bar{\mathbf{I}}^t$  as thermodynamically conjugate variable to the deformation gradient  $\mathbf{F}$  and a reduced dissipation inequality which places implicit restrictions on the dissipation generated by the density evolution  $D_t \rho_0$  through the mass flux  $\mathbf{R}$  and the mass source  $\mathcal{R}_0$ .

$$\bar{\mathbf{I}}^t = \rho_0 D_{\mathbf{F}} \Psi \quad (18a)$$

$$\bar{d}_0 = -\rho_0 D_{\rho_0} \Psi [\text{Div } \mathbf{R} - \mathcal{R}_0] + [\text{Div } \mathbf{S} - \mathcal{S}_0] \theta \geq 0 \quad (18b)$$

#### 3.1. Constitutive equations for biomaterials

A typical specification of the free energy function for cellular materials like open-pored hard tissues is based on an elastic free energy, e.g. of Neo-Hooke type  $\Psi^{\text{neo}}$ , weighted by the actual relative density  $[\rho_0/\rho_0^*]^n$ , see Reference [29] or [30].

$$\Psi = \left[ \frac{\rho_0}{\rho_0^*} \right]^n \Psi^{\text{neo}}, \quad \Psi^{\text{neo}} = \frac{1}{\rho_0} \left[ \frac{1}{2} \lambda \ln^2 J + \frac{1}{2} \mu [\mathbf{b} : \mathbf{1} - 3 - 2 \ln J] \right] \quad (19)$$

Herein,  $\lambda$  and  $\mu$  denote the classical Lamé constants and  $n$  is a characteristic exponent varying between  $1 \leq n \leq 3.5$  according to the corresponding porosity of the material. The derivatives

of the free energy  $\Psi$  with respect to the material density  $\rho_0$  and the deformation gradient  $\mathbf{F}$  take the following format:

$$\begin{aligned}
 D_{\rho_0}\Psi &= [n - 1] \left[ \frac{\rho_0}{\rho_0^*} \right]^{[n-2]} \left[ \frac{1}{\rho_0^*} \right]^2 \left[ \frac{1}{2} \lambda \ln^2 J + \frac{1}{2} \mu [\mathbf{b} : \mathbf{1} - 3 - 2 \ln J] \right] \\
 D_{\mathbf{F}}\Psi &= \left[ \frac{\rho_0}{\rho_0^*} \right]^{[n-1]} \left[ \frac{1}{\rho_0^*} \right] [\mu \mathbf{F} + [\lambda \ln J - \mu] \mathbf{F}^{-t}]
 \end{aligned}
 \tag{20}$$

whereby the first derivative can alternatively be expressed as  $D_{\rho_0}\Psi = [n - 1]\Psi/\rho_0$ . According to Equation (18a), the reduced first Piola–Kirchhoff stress tensor

$$\bar{\mathbf{H}}^t = \left[ \frac{\rho_0}{\rho_0^*} \right]^n [\mu \mathbf{F} + [\lambda \ln J - \mu] \mathbf{F}^{-t}]
 \tag{21}$$

can be understood as the classical Neo-Hookean stress tensor weighted by the actual relative density  $[\rho_0/\rho_0^*]^n$ . For the sake of simplicity, the reduced momentum source  $\bar{\mathbf{b}}_0$  is assumed to vanish identically.

$$\bar{\mathbf{b}}_0 = \mathbf{0}
 \tag{22}$$

The mass flux  $\mathbf{R}$  is assumed to be related to the spatial gradient of the density  $\nabla\rho_0$  weighted by a mass conduction coefficient  $R_0$ . A possible definition of the extra entropy flux  $\mathbf{S}$  follows from the reduced dissipation inequality (18b).

$$\mathbf{R} = R_0 \nabla\rho_0, \quad \mathbf{S} = [n - 1] \Psi \frac{1}{\theta} R_0 \nabla\rho_0
 \tag{23}$$

The above definition of the mass flux vector parallels the definition of the heat flux vector in terms of the temperature gradient and the heat conduction coefficient through Fourier’s law in the case of heat conduction. In complete analogy, the flux of concentrations is introduced in terms of the spatial gradient of the concentration through Fick’s law in chemomechanical applications. The mass conduction coefficient  $R_0$  has the unit of a length squared divided by the time. Just like the gradient parameter in the context of gradient enhanced continuum mechanics, see e.g. Reference [31], the mass conduction coefficient thus introduces a microstructural length into the formulation. In the context of hard tissue mechanics, we typically find variations of the following constitutive equation for the mass source  $\mathcal{R}_0$ ,

$$\mathcal{R}_0 = \left[ \frac{\rho_0}{\rho_0^*} \right]^{-m} \Psi_0 - \Psi_0^*, \quad \mathcal{S}_0 = -[n - 1] \Psi \frac{1}{\theta} \left[ \left[ \frac{\rho_0}{\rho_0^*} \right]^{-m} \Psi_0 - \Psi_0^* \right]
 \tag{24}$$

whereby  $\rho_0^*$  and  $\Psi_0^*$  denote the reference density and the reference free energy, respectively, while  $m$  is an additional exponent that is commonly chosen to  $m > n$ , see Reference [21]. Again, a possible definition for the extra entropy source  $\mathcal{S}_0$  follows from the dissipation inequality (18b). In total, the model is thus defined through seven material parameters, the two Lamé constants  $\lambda$  and  $\mu$  characterizing the elastic behaviour of the basic material, the mass conduction coefficient  $R_0$ , the reference density  $\rho_0^*$ , the reference free energy  $\Psi_0^*$  sometimes also referred to as attractor stimulus and the two exponents  $n$  and  $m$ . The study of the sensitivity towards the choice of the model parameters will be the subject of Section 5.

## 4. FINITE ELEMENT FORMULATION

In the following, we shall illustrate the derivation of a finite element formulation for open systems restricting ourselves to the isothermal case. Consequently, the density  $\rho_0$  and the deformation  $\boldsymbol{\varphi}$  furnish the primary unknowns of the resulting two-field formulation which will be solved in a monolithic sense in the sequel.

## 4.1. Strong form of the coupled boundary value problem

The material density  $\rho_0$  and the deformation map  $\boldsymbol{\varphi}$  are governed by the scalar-valued balance of mass (4) and the vector-valued mass specific balance of linear momentum (4) which can be cast into the residual statements  $\mathbf{R}^\rho = 0$  and  $\mathbf{R}^\varphi = \mathbf{0}$  to be valid in the material domain  $\mathcal{B}_0$ .

$$\mathbf{R}^\rho(\rho_0, \boldsymbol{\varphi}) = D_t \rho_0 - \text{Div } \mathbf{R}(\rho_0, \boldsymbol{\varphi}) - \mathcal{R}_0(\rho_0, \boldsymbol{\varphi}) = 0 \quad \text{in } \mathcal{B}_0 \quad (25a)$$

$$\mathbf{R}^\varphi(\rho_0, \boldsymbol{\varphi}) = \rho_0 D_t \mathbf{p} - \text{Div } \bar{\mathbf{\Pi}}^t(\rho_0, \boldsymbol{\varphi}) - \bar{\mathbf{b}}_0(\rho_0, \boldsymbol{\varphi}) = \mathbf{0} \quad \text{in } \mathcal{B}_0 \quad (25b)$$

Thereby, the boundary  $\partial \mathcal{B}_0$  of the material domain is decomposed into disjoint parts  $\partial \mathcal{B}_0^\rho$  and  $\partial \mathcal{B}_0^r$  for the density problem and equivalently into  $\partial \mathcal{B}_0^\varphi$  and  $\partial \mathcal{B}_0^t$  for the deformation problem.

$$\begin{aligned} \partial \mathcal{B}_0^\rho \cup \partial \mathcal{B}_0^r &= \partial \mathcal{B}_0, & \partial \mathcal{B}_0^\rho \cap \partial \mathcal{B}_0^r &= \emptyset \\ \partial \mathcal{B}_0^\varphi \cup \partial \mathcal{B}_0^t &= \partial \mathcal{B}_0, & \partial \mathcal{B}_0^\varphi \cap \partial \mathcal{B}_0^t &= \emptyset \end{aligned} \quad (26)$$

While Dirichlet boundary conditions are prescribed on  $\partial \mathcal{B}_0^\rho$  and  $\partial \mathcal{B}_0^\varphi$ , Neumann boundary conditions are prescribed for the mass flux and the tractions on  $\partial \mathcal{B}_0^r$  and  $\partial \mathcal{B}_0^t$ .

$$\rho_0 = \bar{\rho}_0 \quad \text{on } \partial \mathcal{B}_0^\rho \quad (27a)$$

$$\mathbf{R}(\rho_0, \boldsymbol{\varphi}) \cdot \mathbf{N} = \bar{\mathbf{r}}^{\text{closed}} + \bar{\mathbf{r}}^{\text{open}} \quad \text{on } \partial \mathcal{B}_0^r \quad (27b)$$

$$\boldsymbol{\varphi} = \bar{\boldsymbol{\varphi}} \quad \text{on } \partial \mathcal{B}_0^\varphi \quad (27c)$$

$$\bar{\mathbf{\Pi}}^t(\rho_0, \boldsymbol{\varphi}) \cdot \mathbf{N} = \bar{\mathbf{t}}^{\text{closed}} + \bar{\mathbf{t}}^{\text{open}} \quad \text{on } \partial \mathcal{B}_0^t \quad (27d)$$

*Remark 4.1*

Note that in the classical literature of biomechanics, the balance of mass (25a) is commonly addressed as ‘biological equilibrium’ while the balance of linear momentum (25b) represents the ‘mechanical equilibrium’ equation.

## 4.2. Weak form of the coupled boundary value problem

The finite element discretization of the above equations requires their reformulation in weak form. To this end, the balance of mass (25a) and the corresponding Neumann boundary conditions (27b) are tested by the scalar-valued test function  $\delta \rho$  while the balance of linear momentum (25b) and the related Neumann boundary conditions (27d) are tested by the

vector-valued test function  $\delta\boldsymbol{\varphi}$ . We thus obtain the weak forms  $G^\rho$  and  $G^\varphi$

$$\begin{aligned} G^\rho(\delta\rho; \rho_0, \boldsymbol{\varphi}) &= 0 \quad \forall \delta\rho \text{ in } H_1^0(\mathcal{B}_0) \\ G^\varphi(\delta\boldsymbol{\varphi}; \rho_0, \boldsymbol{\varphi}) &= 0 \quad \forall \delta\boldsymbol{\varphi} \text{ in } H_1^0(\mathcal{B}_0) \end{aligned} \tag{28}$$

which expand into the following expressions:

$$G^\rho = \int_{\mathcal{B}_0} \delta\rho D_t \rho_0 \, dV + \int_{\mathcal{B}_0} \nabla \delta\rho \cdot \mathbf{R} \, dV - \int_{\partial\mathcal{B}'_0} \delta\rho [r^{\text{closed}} + \bar{r}^{\text{open}}] \, dA - \int_{\mathcal{B}_0} \delta\rho \mathcal{R}_0 \, dV \tag{29a}$$

$$G^\varphi = \int_{\mathcal{B}_0} \delta\boldsymbol{\varphi} \cdot \rho_0 D_t \mathbf{p} \, dV + \int_{\mathcal{B}_0} \nabla \delta\boldsymbol{\varphi} : \bar{\boldsymbol{\Pi}}^t \, dV - \int_{\partial\mathcal{B}'_0} \delta\boldsymbol{\varphi} \cdot [\mathbf{t}^{\text{closed}} + \bar{\mathbf{t}}^{\text{open}}] \, dA - \int_{\mathcal{B}_0} \delta\boldsymbol{\varphi} \cdot \bar{\mathbf{b}}_0 \, dV \tag{29b}$$

By interpreting the vector-valued test function  $\delta\boldsymbol{\varphi}$  as virtual displacements, we typically identify the weak form of the balance of momentum (29b) as the virtual work expression.

### 4.3. Temporal discretization of the coupled boundary value problem

For the temporal discretization of the set of governing equations, consider a partition  $T = \bigcup_{n=0}^{n_{\text{step}}-1} [t_n, t_{n+1}]$  of the time interval of interest  $T$  and focus on the typical time subinterval  $[t_n, t_{n+1}]$  with  $\Delta t := t_{n+1} - t_n > 0$  denoting the corresponding actual time increment. Assume that the primary unknowns  $\rho_{0n}$  and  $\boldsymbol{\varphi}_n$  and all derivable quantities are known at  $t_n$ . Without loss of generality, we shall apply the classical implicit Euler backward time integration scheme to reformulate the set of equations in terms of the unknowns  $\rho_{0n+1}$  and  $\boldsymbol{\varphi}_{n+1}$ .

$$\begin{aligned} G_{n+1}^\rho(\delta\rho; \rho_{0n+1}, \boldsymbol{\varphi}_{n+1}) &= 0 \quad \forall \delta\rho \text{ in } H_1^0(\mathcal{B}_0) \\ G_{n+1}^\varphi(\delta\boldsymbol{\varphi}; \rho_{0n+1}, \boldsymbol{\varphi}_{n+1}) &= 0 \quad \forall \delta\boldsymbol{\varphi} \text{ in } H_1^0(\mathcal{B}_0) \end{aligned} \tag{30}$$

Together with the following approximation of the first-order material time derivatives  $D_t \rho_0$  and  $D_t \mathbf{p}$  as

$$D_t \rho_0 = \frac{1}{\Delta t} [\rho_{0n+1} - \rho_{0n}], \quad D_t \mathbf{p} = \frac{1}{\Delta t} [\mathbf{p}_{n+1} - \mathbf{p}_n] \tag{31}$$

we obtain the semi-discrete virtual work expressions of the balance of mass and linear momentum.

$$\begin{aligned} G_{n+1}^\rho &= \int_{\mathcal{B}_0} \delta\rho \frac{\rho_{0n+1} - \rho_{0n}}{\Delta t} + \nabla \delta\rho \cdot \mathbf{R}_{n+1} \, dV - \int_{\partial\mathcal{B}'_0} \delta\rho [r_{n+1}^{\text{closed}} + \bar{r}_{n+1}^{\text{open}}] \, dA - \int_{\mathcal{B}_0} \delta\rho \mathcal{R}_{0n+1} \, dV \\ G_{n+1}^\varphi &= \int_{\mathcal{B}_0} \delta\boldsymbol{\varphi} \cdot \rho_0 \frac{\mathbf{p}_{n+1} - \mathbf{p}_n}{\Delta t} + \nabla \delta\boldsymbol{\varphi} : \bar{\boldsymbol{\Pi}}_{n+1}^t \, dV - \int_{\partial\mathcal{B}'_0} \delta\boldsymbol{\varphi} \cdot [\mathbf{t}_{n+1}^{\text{closed}} + \bar{\mathbf{t}}_{n+1}^{\text{open}}] \, dA - \int_{\mathcal{B}_0} \delta\boldsymbol{\varphi} \cdot \bar{\mathbf{b}}_{0n+1} \, dV \end{aligned} \tag{32}$$

#### 4.4. Spatial discretization of the coupled boundary value problem

Next, the semi-discrete set of equations is discretized in space with the finite element method. Classically, in the spirit of the finite element method, the underlying domain  $\mathcal{B}_0$  is discretized into  $n_{el}$  elements  $\mathcal{B}_0^e$ , whereby the underlying geometry  $\mathbf{X}$  is interpolated elementwise by the shape functions  $N_X^i$  in terms of the discrete nodal point positions  $\mathbf{X}_i$  of the  $i = 1..n_{en}$  element nodes.

$$\mathcal{B}_0 = \bigcup_{e=1}^{n_{el}} \mathcal{B}_0^e, \quad \mathbf{X}^h|_{\mathcal{B}_0^e} = \sum_{I=1}^{n_{en}} N_X^I \mathbf{X}_I \quad (33)$$

Correspondingly, the global set of all  $n_{np}$  global discretization node points  $\mathbb{B}$  can be abstractly related to the elementwise set of all  $n_{en}$  element nodes  $\mathbb{B}^e$  as  $\mathbb{B} = \bigcup_{e=1}^{n_{el}} \mathbb{B}^e$  with  $\mathbb{B} = \{I \mid I = 1, n_{np}\}$  and  $\mathbb{B}^e = \{i \mid i = 1, n_{en}\}$ . Following the isoparametric concept, the unknowns  $\rho_0$  and  $\boldsymbol{\varphi}$  are interpolated on the element level with the same shape functions  $N_\rho^i$  and  $N_\varphi^j$  as the element geometry  $\mathbf{X}$ . These shape functions are also applied to interpolate the test functions  $\delta\rho$  and  $\delta\boldsymbol{\varphi}$  in the spirit of the Bubnov–Galerkin technique.

$$\begin{aligned} \delta\rho^h|_{\mathcal{B}_0^e} &= \sum_{i=1}^{n_{en}} N_\rho^i \delta\rho_i \in H_1^0(\mathcal{B}_0), & \rho_0^h|_{\mathcal{B}_0^e} &= \sum_{k=1}^{n_{en}} N_\rho^k \rho_k \in H_1(\mathcal{B}_0) \\ \delta\boldsymbol{\varphi}^h|_{\mathcal{B}_0^e} &= \sum_{j=1}^{n_{en}} N_\varphi^j \delta\boldsymbol{\varphi}_j \in H_1^0(\mathcal{B}_0), & \boldsymbol{\varphi}^h|_{\mathcal{B}_0^e} &= \sum_{l=1}^{n_{en}} N_\varphi^l \boldsymbol{\varphi}_l \in H_1(\mathcal{B}_0) \end{aligned} \quad (34)$$

Correspondingly, the discretization of the related gradients of the test functions  $\nabla\delta\rho^h$  and  $\nabla\delta\boldsymbol{\varphi}^h$  and the gradients of the primary unknowns  $\nabla\rho^h$  and  $\nabla\boldsymbol{\varphi}^h$  takes the following elementwise format.

$$\begin{aligned} \nabla\delta\rho^h|_{\mathcal{B}_0^e} &= \sum_{i=1}^{n_{en}} \delta\rho_i \nabla N_\rho^i, & \nabla\rho_0^h|_{\mathcal{B}_0^e} &= \sum_{k=1}^{n_{en}} \rho_k \nabla N_\rho^k \\ \nabla\delta\boldsymbol{\varphi}^h|_{\mathcal{B}_0^e} &= \sum_{j=1}^{n_{en}} \delta\boldsymbol{\varphi}_j \otimes \nabla N_\varphi^j, & \nabla\boldsymbol{\varphi}^h|_{\mathcal{B}_0^e} &= \sum_{l=1}^{n_{en}} \boldsymbol{\varphi}_l \otimes \nabla N_\varphi^l \end{aligned} \quad (35)$$

Although it is in principle possible to choose different expansions for the density  $\rho_0$  and the deformation  $\boldsymbol{\varphi}$ , we shall apply an equal order interpolation technique in the sequel which has been proven to yield reasonable results. Based on the above described discretization of the primary unknowns, the discrete algorithmic balance of mass and momentum follows as,

$$\begin{aligned} \mathbf{R}_I^\rho(\rho_{0n+1}^h, \boldsymbol{\varphi}_{n+1}^h) &= 0 \quad \forall I \text{ in } \mathbb{B} \\ \mathbf{R}_J^\varphi(\rho_{0n+1}^h, \boldsymbol{\varphi}_{n+1}^h) &= \mathbf{0} \quad \forall J \text{ in } \mathbb{B} \end{aligned} \quad (36)$$

whereby the discrete scalar-valued residuum of the balance of mass  $\mathbf{R}_I^\rho$  and the discrete vector-valued residuum of the balance of momentum  $\mathbf{R}_J^\varphi$  expand to the following expressions:

$$\mathbf{R}_I^\rho = \mathbf{A} \int_{\mathcal{B}_0^e} N_\rho^i \frac{\rho_{0n+1} - \rho_{0n}}{\Delta t} + \nabla N_\rho^i \cdot \mathbf{R}_{n+1} \, dV - \int_{\partial\mathcal{B}_0^{er}} N_\rho^i [r_{n+1}^{\text{closed}} + \bar{r}_{n+1}^{\text{open}}] \, dA - \int_{\mathcal{B}_0^e} N_\rho^i \mathcal{R}_{0n+1} \, dV \quad (37a)$$

$$\mathbf{R}_J^\phi = \mathbf{A} \int_{\mathcal{B}_0^e}^{n_{el}} N_\phi^j \rho_0 \frac{\mathbf{p}_{n+1} - \mathbf{p}_n}{\Delta t} + \nabla N_\phi^j \cdot \bar{\mathbf{\Pi}}_{n+1} \, dV - \int_{\partial \mathcal{B}_0^e} N_\phi^j [\mathbf{t}_{n+1}^{\text{closed}} + \bar{\mathbf{t}}_{n+1}^{\text{open}}] \, dA - \int_{\mathcal{B}_0^e} N_\phi^j \bar{\mathbf{b}}_{0n+1} \, dV \tag{37b}$$

Herein, the operator  $\mathbf{A}$  denotes the assembly of all element contributions at the element nodes  $i, j = 1, n_{en}$  to the overall residuals at the global node points  $I, J = 1, n_{np}$ .

4.5. Linearization of the coupled boundary value problem

Equations (37) represent the governing discrete non-linear coupled system of equations. It can be solved efficiently by applying a monolithic incremental iterative solution strategy in the spirit of the Newton–Raphson technique. To this end, we perform a consistent linearization of the governing equations at time  $t_{n+1}$ ,

$$\begin{aligned} \mathbf{R}_{In+1}^{\rho k+1} &= \mathbf{R}_{In+1}^{\rho k} + d\mathbf{R}_I^\rho \doteq \mathbf{0} \quad \forall I \text{ in } \mathbb{B} \\ \mathbf{R}_{Jn+1}^{\phi k+1} &= \mathbf{R}_{Jn+1}^{\phi k} + d\mathbf{R}_J^\phi \doteq \mathbf{0} \quad \forall J \text{ in } \mathbb{B} \end{aligned} \tag{38}$$

whereby the iterative residua  $d\mathbf{R}_I^\rho$  and  $d\mathbf{R}_J^\phi$

$$\begin{aligned} d\mathbf{R}_I^\rho &= \sum_{K=1}^{n_{np}} \mathbf{K}_{\rho\rho}^{IK} d\rho_K + \sum_{L=1}^{n_{np}} \mathbf{K}_{\rho\phi}^{IL} \cdot d\boldsymbol{\phi}_L \quad \forall I \text{ in } \mathbb{B} \\ d\mathbf{R}_J^\phi &= \sum_{K=1}^{n_{np}} \mathbf{K}_{\phi\rho}^{JK} d\rho_K + \sum_{L=1}^{n_{np}} \mathbf{K}_{\phi\phi}^{JL} \cdot d\boldsymbol{\phi}_L \quad \forall J \text{ in } \mathbb{B} \end{aligned} \tag{39}$$

can be expressed in terms of the iteration matrices  $\mathbf{K}_{\rho\rho}^{IK}$ ,  $\mathbf{K}_{\rho\phi}^{IL}$ ,  $\mathbf{K}_{\phi\rho}^{JK}$  and  $\mathbf{K}_{\phi\phi}^{JL}$  which take the interpretation as global tangential stiffness matrix. For the problem at hand, these iteration matrices take the following format:

$$\mathbf{K}_{\rho\rho}^{IK} = \mathbf{A} \int_{\mathcal{B}_0}^{n_{el}} N^i \frac{1}{\Delta t} N^k \, dV - \int_{\mathcal{B}_0} N^i \partial_{\rho_0} \mathcal{R}_0 N^k \, dV + \int_{\mathcal{B}_0} \nabla N^i \cdot R_0 \nabla N^k \, dV \tag{40a}$$

$$\mathbf{K}_{\rho\phi}^{IL} = \mathbf{A} - \int_{\mathcal{B}_0}^{n_{el}} N^i \partial_{\mathbf{F}} \mathcal{R}_0 \cdot \nabla N^l \, dV \tag{40b}$$

$$\mathbf{K}_{\phi\rho}^{JK} = \mathbf{A} \int_{\mathcal{B}_0}^{n_{el}} \nabla N^j \cdot \partial_{\rho_0} \bar{\mathbf{\Pi}}^l N^k \, dV \tag{40c}$$

$$\mathbf{K}_{\phi\phi}^{JL} = \mathbf{A} \int_{\mathcal{B}_0}^{n_{el}} N^j \rho_0 \frac{1}{\Delta t} \mathbf{I} N^l \, dV + \int_{\mathcal{B}_t} \nabla N^j \cdot \partial_{\mathbf{F}} \bar{\mathbf{\Pi}} \cdot \nabla N^l \, dV \tag{40d}$$

Finally, the iterative update for the incrementals of the global unknowns  $\rho_I$  and  $\boldsymbol{\phi}_J$

$$\begin{aligned} \Delta \rho_I &= \Delta \rho_I + d\rho_I \quad \forall I \text{ in } \mathbb{B} \\ \Delta \boldsymbol{\phi}_J &= \Delta \boldsymbol{\phi}_J + d\boldsymbol{\phi}_J \quad \forall J \text{ in } \mathbb{B} \end{aligned} \tag{41}$$

can be expressed in terms of the solution of the linearized system of Equations (38).

*Remark 4.2*

In order to avoid numerical problems caused by the different time scales of the biological and the mechanical problem, the balance of linear momentum is typically considered in a quasi-static sense by neglecting the corresponding dynamic contributions which manifest themselves in the transient term  $N_\varphi^j \rho_0 [\mathbf{p}_{n+1} - \mathbf{p}_n] / \Delta t$  of Equation (37b) and the  $N^j \rho_0 / \Delta t \mathbf{I} N^l$  term of Equation (40d).

*Remark 4.3*

To avoid an ill-conditioned system of equations, it might seem reasonable to scale the balance of mass by the initial density  $\rho_0^*$  and introduce the relative density  $[\rho_0 / \rho_0^*]$  as primary unknown, see e.g. Reference [27]. Within the present formulation, scaling has been performed in such a way, that the relative change in density  $[\rho_0 - \rho_0^*] / \rho_0^*$  rather than the density itself is introduced as primary variable. As an advantage of this particular form of scaling, negative values  $-1 < [\rho_0 - \rho_0^*] / \rho_0^* < 0$  characterize material resorption while positive values  $0 < [\rho_0 - \rho_0^*] / \rho_0^* < \infty$  indicate the absorption of new material.

## 5. PROTOTYPE EXAMPLES

## 5.1. One-dimensional model problem: influence of mass source

In the first example, we shall illustrate the sensitivity of the density evolution with respect to the parameters characterizing the mass source  $\mathcal{R}_0$ . To this end, we shall assume the mass flux to vanish identically as  $\mathbf{R} = \mathbf{0}$  and the balance of mass takes the following simple format:

$$D_t \rho_0 = \mathcal{R}_0 \quad \text{with} \quad \mathcal{R}_0 = \left[ \frac{\rho_0}{\rho_0^*} \right]^{-m} \Psi_0 - \Psi_0^*$$

We consider a one-dimensional homogeneous specimen of unit size with an elasticity modulus of  $E = 1$  and a Poisson's ratio of  $\nu = 0$ . Unless otherwise stated, the reference density is chosen to  $\rho_0^* = 1$ , the value of the reference free energy is  $\Psi_0^* = 1$  and the two exponents are chosen as  $n = 2$  and  $m = 3$  while no mass flux is assumed to take place as  $R_0 = 0$ . The time integration is performed with time increments of  $\Delta t = 0.1$  if not stated otherwise. The specimen is loaded by a multiple step loading function with  $f = 0.5$  N for  $0.0 \leq t \leq 2.0$ ,  $f = 1.0$  N for  $2.0 < t \leq 4.0$ ,  $f = 1.5$  N for  $4.0 < t \leq 6.0$  and finally  $f = 2.0$  N for  $6.0 < t \leq 8.0$ , compare Figure 2(a). The corresponding deformation illustrated in Figure 1

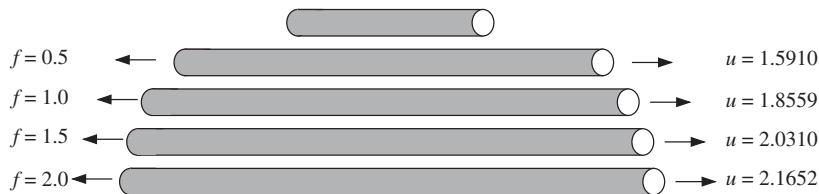


Figure 1. One-dimensional model problem.

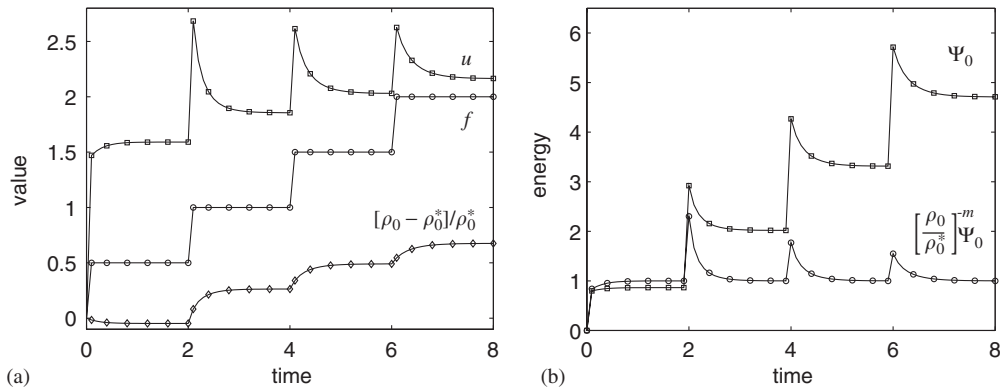


Figure 2. Temporal evolution of density  $\rho_0$ , displacements  $u$  and energy values  $\Psi$  and  $[\rho_0/\rho_0^*]^{-m}\Psi$ .

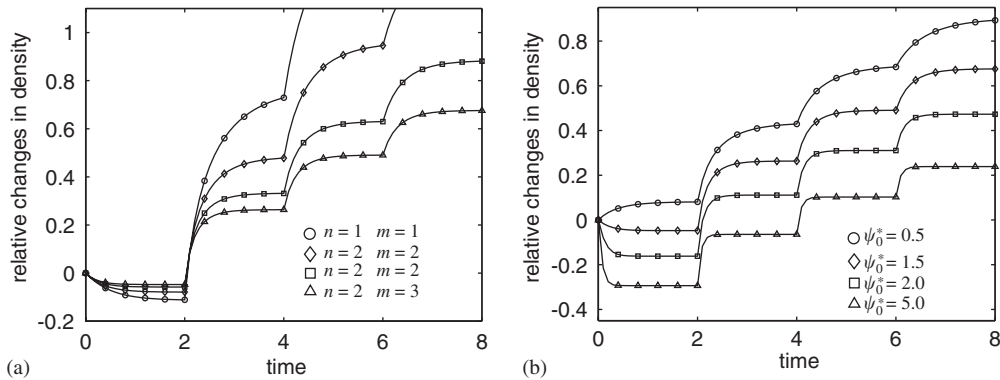


Figure 3. Parameter sensitivity with respect to  $n$ ,  $m$  and  $\Psi_0^*$ .

clearly reflects the non-linearity of the problem introduced on the one hand through the coupling and on the other hand through the geometric non-linearity itself.

The time-dependent nature of the balance of mass is visualized in Figures 2(a) and (b). The former depicts the evolution of the primary unknowns, the relative changes in material density  $[\rho_0 - \rho_0^*]/\rho_0^*$  and the displacements  $u$  for the prescribed loading history  $f$  while the latter shows the resulting evolution of the free energy  $\Psi_0$  and the ‘biological stimulus’  $[\rho_0/\rho_0^*]^{-m}\Psi_0$ . All curves obviously demonstrate the relaxation of the corresponding quantities towards ‘biological equilibrium’, the state at which the density distribution has converged to a final equilibrium value. Each increase of the loading  $f$  is followed by changes in the primary unknowns converging towards a new equilibrium state.

Figures 3(a) and (b) illustrate the sensitivity of the evolution of relative changes in density  $[\rho_0 - \rho_0^*]/\rho_0^*$  with respect to changes in the exponents  $n$  and  $m$  and the reference value of the free energy  $\Psi_0^*$ . It is clearly visible, that the amount of change in density increases with increasing exponents  $n$  and  $m$ . For  $n=2$  and  $m=3$  the relative change in density is inversely

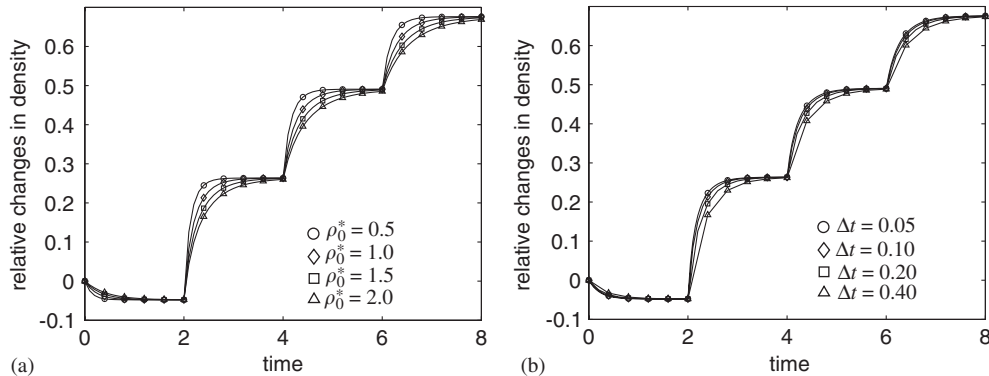


Figure 4. Parameter sensitivity with respect to  $\rho_0^*$  and  $\Delta t$ .

proportional to the reference free energy  $\Psi_0^*$  as  $[\rho_0 - \rho_0^*]/\rho_0^* = \Psi_0^{neo}/\Psi_0^* - 1$ . Its value thus increases for decreasing values of  $\Psi_0^*$  as illustrated in Figure 3(b).

Figures 4(a) and (b) demonstrate the remarkable fact, that for the chosen exponents of  $n=2$  and  $m=3$ , the equilibrium value of the relative change in density  $[\rho_0 - \rho_0^*]/\rho_0^*$  is not only insensitive to changes in the reference density  $\rho_0^*$  as  $[\rho_0 - \rho_0^*]/\rho_0^* = \Psi_0^{neo}/\Psi_0^* - 1$  but also insensitive to the choice of the time step  $\Delta t$ . Nevertheless, both,  $\Psi_0^*$  and  $\Delta t$  influence the rate of convergence towards this value of equilibrium. Convergence is thus faster for smaller initial densities  $\rho_0^*$  and smaller time steps  $\Delta t$ .

5.2. One-dimensional model problem: influence of mass flux

The second example demonstrates the sensitivity of the solution with respect to the mass flux. Consequently, we neglect the mass source as  $\mathcal{R}_0=0$ . The balance of mass

$$D_t \rho_0 = \text{Div } \mathbf{R} \quad \text{with } \mathbf{R} = R_0 \nabla \rho_0$$

thus fully decouples from the balance of momentum. We assume an initial hat-type distribution of the density with values of  $\rho_0 = 1$  and  $2$  as depicted in Figure 5, bottom left, for  $t=0$ . Thereby, the area of high initial density of 50% of the total specimen length is situated right in the middle of the bar. The corresponding density evolution characterized through the outflux of mass driven by a mass conduction coefficient of  $R_0 = 1.0$  is illustrated in Figure 5. As time proceeds, mass flows out of the areas of high initial mass concentration. After  $t=500$ , a state of equilibrium is reached, for which the mass is distributed uniformly at  $\rho_0 = 1.5$  in the entire domain. An increase of either the mass conduction coefficient  $R_0$  or the time step  $\Delta t$  tends to speed up this process of equalization of the mass concentration.

5.3. One-dimensional model problem: influence of mass source and mass flux

Finally, we consider a one-dimensional specimen whereby both, a mass source and a mass flux are present.

$$D_t \rho_0 = \text{Div } \mathbf{R} + \mathcal{R}_0 \quad \text{with } \mathcal{R}_0 = \left[ \frac{\rho_0}{\rho_0^*} \right]^{-m} \Psi_0 - \Psi_0^* \quad \text{and } \mathbf{R} = R_0 \nabla \rho_0$$

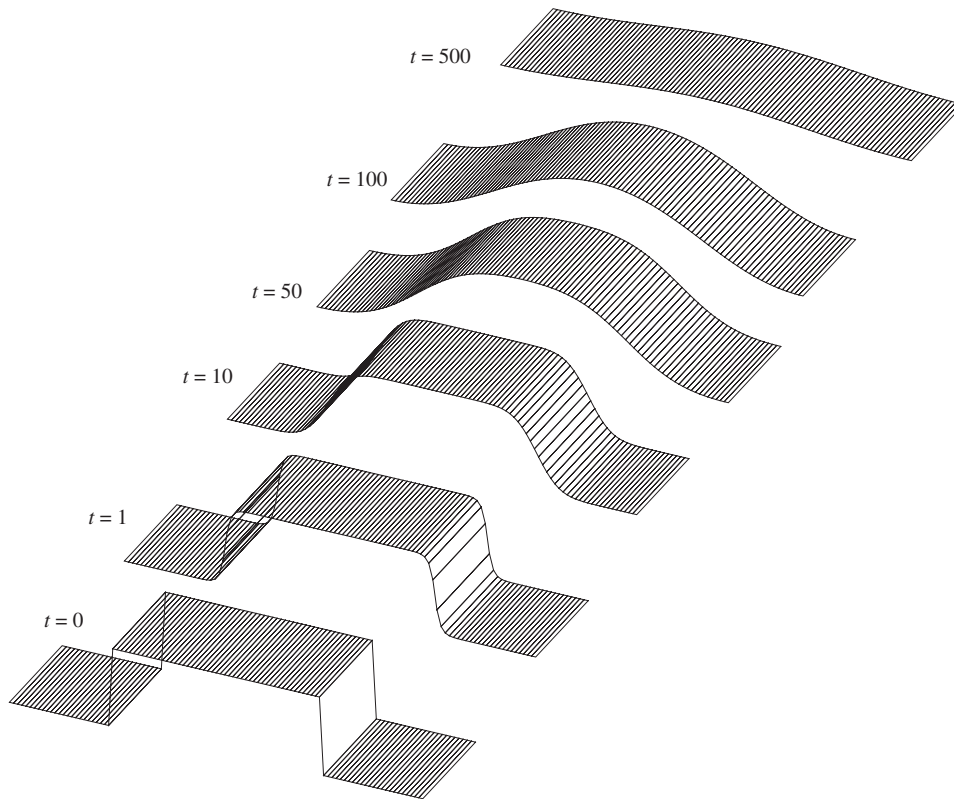


Figure 5. Time evolution of density due to outflux of mass.

In order to perturb the homogeneous solution, the reference value of the free energy, the attractor stimulus  $\Psi_0^*$  has been reduced to  $\Psi_0^* = 1$  in an area of 20% of the total specimen length in the middle of the bar, while it takes values of  $\Psi_0^* = 2$  outside this area. The other material parameters take homogeneous values throughout the specimen with  $E = 1$ ,  $\nu = 0$ ,  $\rho_0^* = 1$ ,  $n = 2$  and  $m = 3$ .

Figure 6 documents the influence of the mass conduction coefficient  $R_0$  which is gradually increased from  $R_0 = 0$  to 1. The depicted density distributions of the different simulations correspond to the converged equilibrium states after 50 time steps of  $\Delta t = 0.1$  each. The discontinuity in the reference free energy  $\Psi_0^*$  induces a non-homogeneous density distribution with maximum values in the middle of the specimen. For  $R_0 = 0$ , the analytical solution corresponds to a hat-type discontinuous density distribution which typically cannot be captured by the  $\mathcal{C}^0$ -continuous finite element simulation. The simulation with  $R_0 = 0$  and thus without mass flux produces density oscillations close to the density jump. Recall, that the discontinuous distribution of material parameters analysed herein represents an extreme test case from an algorithmic point of view. Basically all existing bone remodelling algorithms in biomechanics *a priori* neglect the flux of mass with  $R_0$  being identical to zero throughout. In most practical applications, however, the material parameters do not vary discontinuously in space. Thus,

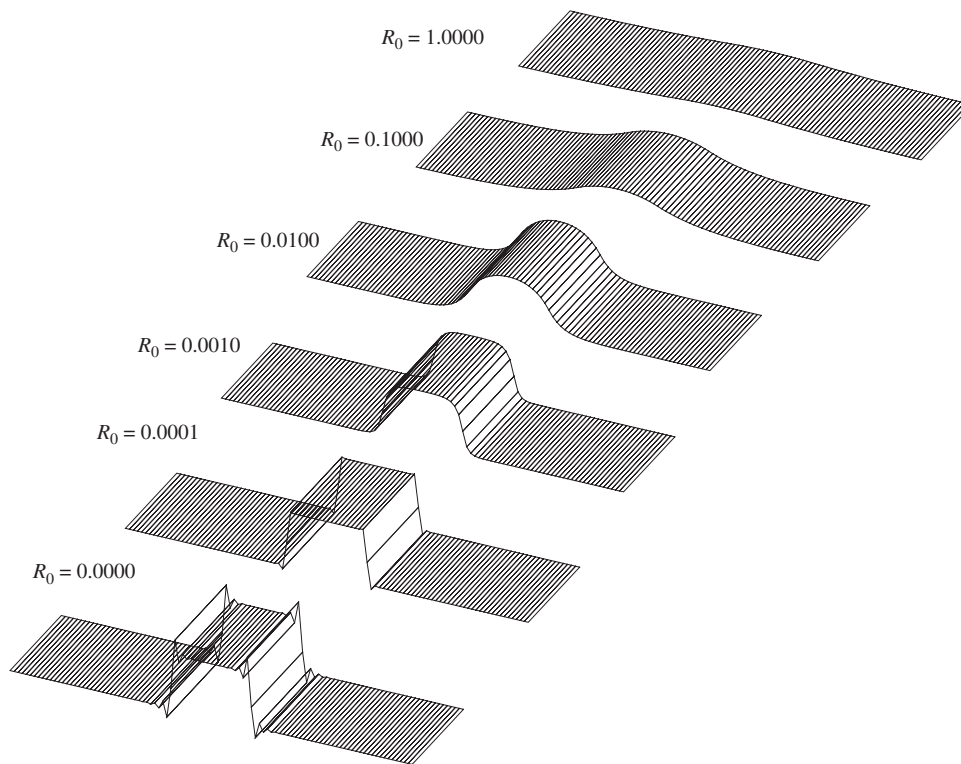


Figure 6. Parameter sensitivity with respect to  $R_0$ .

the potential drawback of a non-diffusive formulation is typically not visible in the examples studied in the literature.

Figure 6 illustrate how the inclusion of the mass flux through the increase of the mass conduction coefficient smoothes the density profile. The area affected by the disturbed material parameter increases considerably with increasing mass conduction coefficients while the gradients of the density decrease. Since the mass conduction coefficient  $R_0$  operates on a Laplacian term, it automatically introduces an additional length scale into the formulation with  $R_0$  having the unit of a microstructural length squared divided by the time. In this respect, the mass conduction coefficient takes an analogous interpretation as the gradient parameter in gradient enhanced continuum mechanics. The effect of smoothing of the density distribution and the characteristic size effect of microstructural materials like hard tissues are thus incorporated in the proposed model in a natural and physically justified way.

## 6. EXAMPLES FROM STRUCTURAL MECHANICS

### 6.1. Topology optimization: influence of mass source

The following example is motivated by the work of Weng [32], who applied an algorithm for the functional adaption of hard tissues to find the optimal arrangement of material in a

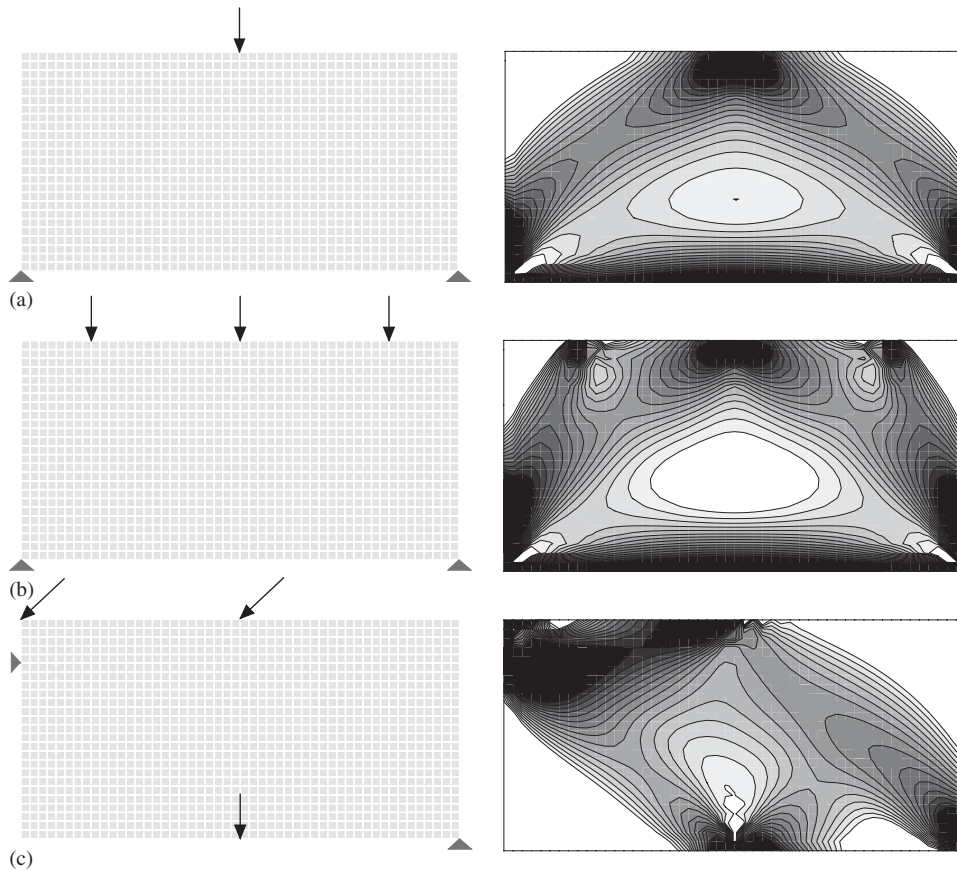


Figure 7. Topology optimization: design space and density distribution for load cases 1, 2 and 3.

rectangular panel under prescribed loads, see Figures 7(a) and (b). A similar example has been analysed by Maute [23] in the context of the topology optimization by aiming at finding the optimal structure of a bicycle frame, see Figure 7(c).

The elastic parameters of the simulation are chosen to  $E = 1000$  and  $\nu = 0.30$ . Changes in density are caused by a density source defined through  $\rho_0^* = 0.1$  and  $\Psi_0^* = 0.5$  in combination with the two exponents  $n = 2$  and  $m = 3$ . In the first part of the example, the flux of density is assumed to be suppressed as  $R_0 = 0$ . The design space of the panels of 1 m length and 0.5 m height as well as the three different types of loading and boundary conditions are depicted in Figure 7(a)–(c). The load is applied as a single step load in the first time step and then held constant throughout the analysis. The simulation is carried out until the density distribution has completely adapted to the applied loading scenario. In the cases considered herein, this state of convergence is achieved after 20 time steps of  $\Delta t = 0.01$ . The resulting density distributions for the three different loading situations are depicted on the right-hand side of Figure 7. Thereby, the white areas indicate a decrease in local density caused by a resorption of material up to  $-80\%$ , while the black areas indicate an increase in local density

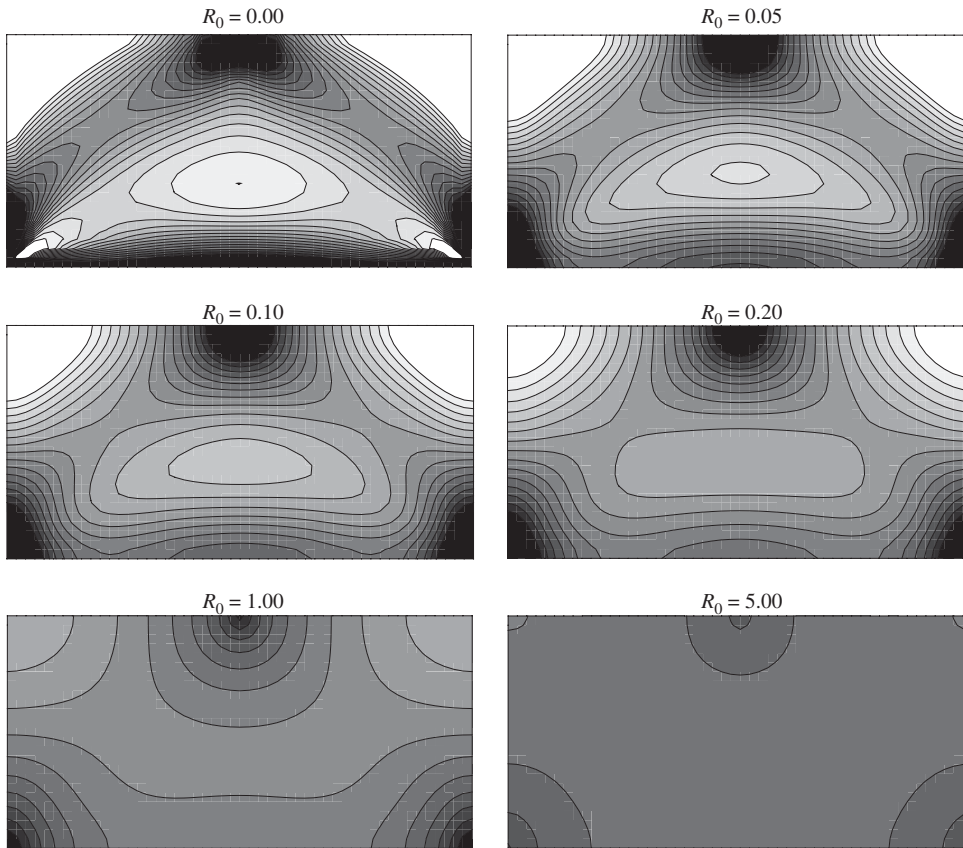


Figure 8. Topology optimization: smoothing influence of mass flux.

and thus the absorption of new material up to +20%. The algorithm clearly tends to build strut-like structures by resorbing material in regions that do not contribute to the load transfer while absorbing material in load carrying areas. Mass is thus locally added in regions where the driving force  $[\rho_0^*/\rho_0]^m \Psi_0$  exceeds the given attractor stimulus  $\Psi_0^*$  while mass is removed locally where the driving force takes values below the attractor stimulus.

The results of the simulations are in good qualitative agreement with the results of Weng [32] and Maute [33]. However, since the density  $\rho_0$  is not introduced as primary unknown on the nodal level but rather determined in a post-processing step, the algorithm for topology optimization introduced by Maute [33] tends to form sharper contours of struts. In the context of topology optimization, the intensity of these contours strongly depends on the type of smoothing function that is typically included in the optimization algorithm.

### 6.2. Topology optimization: influence of mass source and mass flux

Within the present theory, a physically motivated smoothing effect is introduced through the incorporation of the mass flux. Figure 8 contrasts six different simulations of the first frame

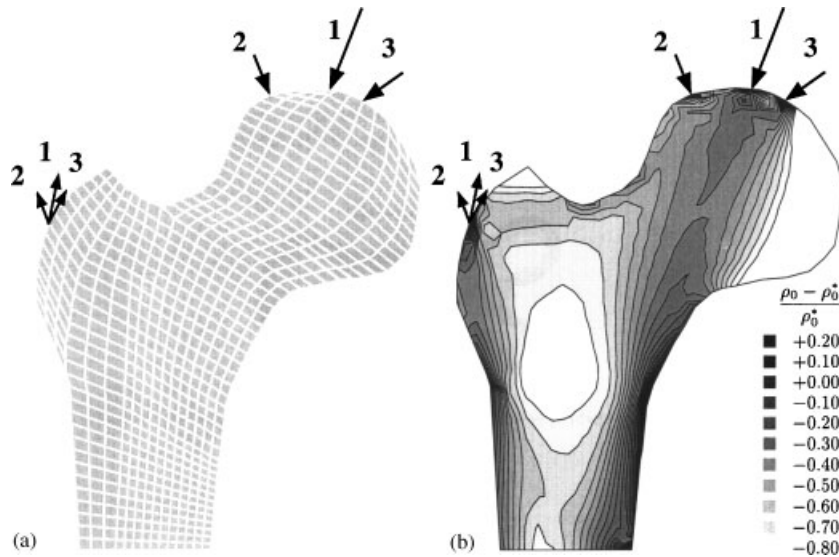


Figure 9. Functional adaption: geometry, loading and density distribution.

depicted in Figure 7(a) whereby the mass conduction coefficient  $R_0$  has been gradually increased from  $R_0=0.00$  to  $5.00$ . The smoothing effect of the mass flux is clearly visible. The larger the mass conduction coefficient, the wider the affected zone and the smoother the contours of the density distribution. In the limit case, which is achieved if the value of  $R_0$  is chosen large enough, even a homogeneous density distribution can be found.

### 7. EXAMPLES FROM BIOMECHANICS

#### 7.1. Functional adaption: influence of mass source

The second example is the functional adaption of the proximal femur, a classical example in biomechanical applications. The material data and the loading conditions are specified e.g. Reference [25]. For the model suggested herein, we have additionally applied the model parameters  $n=2$ ,  $m=3$ ,  $R_0=0$  and  $\Delta t=0.02$ . The underlying geometry as depicted in Figure 9(a) is based on a two-dimensional slice through the proximal femur in the midfrontal plane. The bone density is assumed to be homogeneous at the beginning of the simulation with  $\rho_0^*=1.20$  while the attractor stimulus is chosen to  $\Psi_0^*=0.01$ . Typically, three different load cases can be distinguished. Load case 1 corresponds to the load condition for the mid-distance phase of gait, while load cases 2 and 3 represent the extreme cases of abduction and adduction defined in Table I.

Figure 9(b) shows the predicted density distribution under the assumption of all three load cases. In the femoral head, a column of dense cancelous bone develops along the principal load path from the superior dome of the head. A secondary arcuate system is formed connecting the primary trabecular system to the junction of the superior neck. These observations clearly

Table I. Functional adaption: loading conditions on proximal femur.

Load case	Type of loading	Value (N)	Direction (deg)	Value (N)	Direction (deg)
1	Midstance phase of gait	2317	24	703	28
2	Extreme range of abduction	1158	-15	351	-8
3	Extreme range of adduction	1548	56	468	35

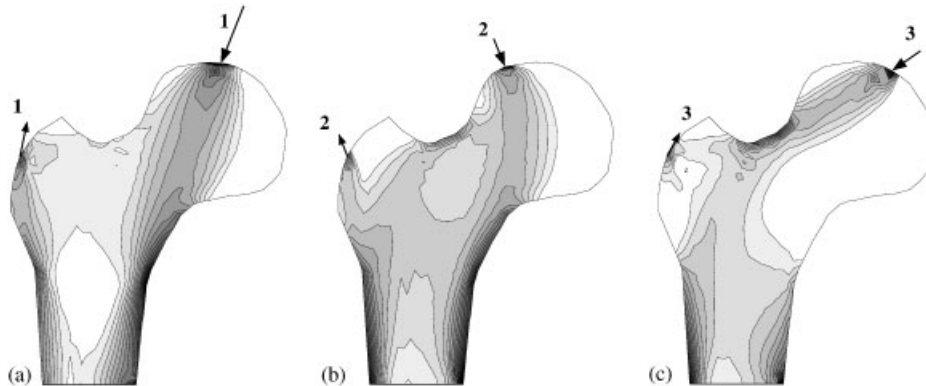


Figure 10. Functional adaption: density distribution for load cases 1, 2 and 3.

match the experimental observations found in radiography of the healthy adult proximal femur, compare e.g. Reference [25] or the early studies of Wolff [1]. In between these two regions of high density, we expect a region of low density known as Ward's triangle. In our simulations, this region indicated by the large white area of low density develops as well, however, it is slightly shifted downward in comparison to anatomical specimens. Distally, in the transitional region between the metaphysis and the diaphysis, we clearly observe the classical low density medullary core surrounded by dense media and lateral cortices.

Figure 10 illustrate the sensitivity of the density distribution with respect to the prescribed loading situation. For the application of load case 1 depicted in Figure 10(a), we observe the formation of a strong system of dense bone that transmits the applied joint force directly into the calcar. Load cases 2 and 3 alone stimulate bone absorption in completely different regions of the proximal femur as illustrated in Figures 10(b) and (c). These results show, that a detailed knowledge of the actual loading situation is elementary to provide a good prediction of the bone architecture. Since the real loading situation is often difficult to access, the proposed algorithm could be applied in an inverse manner in the sense that for a given radiography, one could solve the inverse problem to determine the underlying loading situation.

### 7.2. Functional adaption: influence of mass source and mass flux

The final example shows the qualitative influence of the incorporation of the mass flux, which has so far been neglected in biomechanical analysis of hard tissues. The study is motivated by the famous monograph by Galileo [34] who observed already more than three

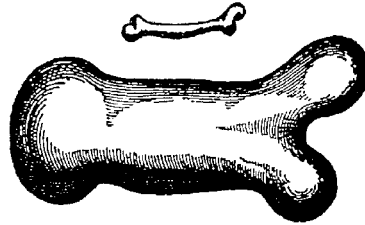


Figure 11. Functional adaption: size effect in bones as predicted by Galileo [34].

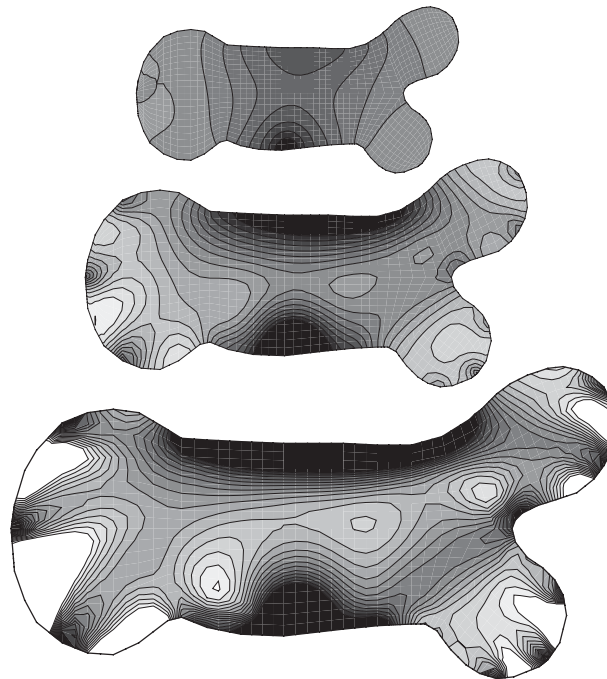


Figure 12. Functional adaption: size effect in bones as predicted by the algorithm.

centuries ago, that bone is a microstructural material. Bone thus shows the classical size effect with smaller structures being relatively stronger than larger ones, see Figure 11. Figure 12 shows the result of the simulation of the Galileo bone subjected to a hypothetical loading situation. To study the formation of microstructures, both, the geometry and the amount of loading have been scaled by a factor 0.5 and 2.0. Thereby, the material parameters, in particular the mass conduction coefficient  $R_0 = 0.1$ , have been held constant. The resulting density distributions clearly demonstrate the fact, that the proposed model is able to capture the characteristic size effect of microstructural materials in a natural way. The larger structure is characterized through the formation of sharp microstructures while the small bone shows a diffuse almost homogeneous density distribution. However, if the mass flux is neglected as

$R_0 = 0$  the predicted density distribution is completely identical for the different bone sizes. The additional incorporation of the mass flux can thus be interpreted as a natural extension of the existing models that enables the simulation of microstructural effects in a physically motivated way.

## 8. CONCLUSION

The present work deals with the theoretical and numerical elaboration of open systems typically encountered in biomechanical or chemomechanical applications. To set the stage, we have briefly reviewed the balance equations of open system thermodynamics. In contrast to existing models, the interaction of the open system with the ‘outside world’ has not *a priori* been restricted to volume terms but rather volume and surface interactions have been taken into account. The governing equations of the overall problem, namely the balance of mass and the mass specific balance of momentum, were suggested to be solved monolithically on the basis of a two-field finite element formulation in terms of the relative density and the material placements as primary unknowns.

The constitutive equations for biomaterials, in particular the constitutive assumptions for the mass source and the mass flux, have been studied in detail for one-dimensional prototype examples. Next, the features of the resulting algorithm were tested qualitatively in the context of topology optimization as a classical example of structural mechanics. Finally, the algorithm has been applied to predict the functional adaption of hard tissues as a typical example of biomechanical applications. All results were in good qualitative agreement with the results documented in the literature. Moreover, the proposed algorithm was shown to incorporate the classical size effect characteristic for microstructural materials through the additional incorporation of the mass flux. Owing to the underlying geometrically exact formulation the proposed algorithm is believed to be particularly suited to model adaptive processes not only in hard but also in soft tissue mechanics which is typically accompanied by large deformations and large strains.

## ACKNOWLEDGEMENTS

The present research is financed by the German Science Foundation DFG through the habilitation grant KU-1313 ‘Aspekte der geometrisch nichtlinearen funktionalen Adaption biologischer Mikrostrukturen’. This support is gratefully acknowledged.

## REFERENCES

1. Wolff J. *Das Gesetz der Knochentransformations*. Hirschwald: Berlin, 1892.
2. Taber LA. Biomechanics of growth, remodeling, and morphogenesis. *Applied Mechanics Reviews* (ASME) 1995; **48**:487–545.
3. Cowin SC. How is a tissue build? *Journal of Biomechanical Engineering* (ASME) 2000; **122**:553–569.
4. Humphrey JD, Rajagopal KR. A constrained mixture model for growth and remodeling of soft tissues. *Mathematical Models and Methods in Applied Sciences* 2002; **12**:407–430.
5. Goldstein H. *Classical Mechanics*. Addison-Wesley: Reading, MA, 1950.
6. Müller I. *Grundzüge der Thermodynamik*. Springer: Berlin, 1994.
7. Haupt P. *Continuum Mechanics and Theory of Materials*. Springer: Berlin, 1999.
8. Maugin GA. *The Thermomechanics of Nonlinear Irreversible Behaviors*. World Scientific: Singapore, 1998.

9. Truesdell C, Toupin R. The classical field theories. In *Handbuch der Physik*, Flügge S (ed.), Vol. III/1. Springer: Berlin, 1960.
10. Bowen RM. Theory of mixtures. In *Continuum Physics—Volume III—Mixtures and EM Field Theories*, Eringen AC (ed.). Academic Press: New York, 1976; 1–127.
11. Ehlers W. Grundlegende Konzepte in der Theorie poröser Medien. *Technische Mechanik* 1996; **16**:63–76.
12. Cowin SC, Hegedus DH. Bone remodelling I: Theory of adaptive elasticity. *Journal of Elasticity* 1976; **6**: 313–326.
13. Epstein M, Maugin GA. Thermomechanics of volumetric growth in uniform bodies. *International Journal of Plasticity* 2000; **16**:951–978.
14. Kuhl E, Steinmann P. On spatial and material settings of thermo-hyperelastodynamics for open systems. *Acta Mechanica* 2002; **160**:179–217.
15. Kuhl E, Steinmann P. Mass and volume specific views on thermodynamics for open systems. *Proceedings of the Royal Society London*, in press.
16. Beaupré GS, Orr TE, Carter DR. An approach for time-dependent bone modelling and remodelling. *Journal of Orthopaedic Research* 1990; **8**:651–670.
17. Jacobs CR, Levenston ME, Beaupré GS, Simo JC, Carter DR. Numerical instabilities in bone remodeling simulations: The advantages of a node-based finite element approach. *Journal of Biomechanics* 1995; **28**: 449–459.
18. Jacobs CR, Simo JC, Beaupré GS, Carter DR. Adaptive bone remodeling incorporating simultaneous density and anisotropy considerations. *Journal of Biomechanics* 1997; **30**:603–613.
19. Weinans H, Huiskes R, Grootenboer HJ. The behavior of adaptive bone-remodeling simulation models. *Journal of Biomechanics* 1992; **25**:1425–1441.
20. Harrigan TP, Hamilton JJ. Optimality condition for finite element simulation of adaptive bone remodeling. *International Journal of Solids and Structures* 1992; **29**:2897–2906.
21. Harrigan TP, Hamilton JJ. Finite element simulation of adaptive bone remodelling: a stability criterion and a time stepping method. *International Journal for Numerical Methods in Engineering* 1993; **36**:837–854.
22. Pettermann HE, Reiter TJ, Rammerstorfer FG. Computational simulation of internal bone remodeling. *Archives of Computational Methods in Engineering* 1997; **4**(4):295–323.
23. Reiter TJ. *Functional Adaption of Bone and Application in Optimal Structural Design*. VDI Berichte Reihe 17, No. 145, VDI-Verlag: Düsseldorf, 1996.
24. Krstin N, Nackenhorst U, Lammering R. Zur konstitutiven Beschreibung des anisotropen beanspruchungs-sadaptiven Knochenumbaus. *Technische Mechanik* 2000; **20**:31–40.
25. Carter DR, Beaupré GS. *Skeletal Function and Form—Mechanobiology of Skeletal Development, Aging and Regeneration*. Cambridge University Press: Cambridge, 2001.
26. Weinans H, Huiskes R, Grootenboer HJ. Effects of fit and bonding characteristics of femoral stems on adaptive bone remodeling. *Journal of Biomechanical Engineering (ASME)* 1994; **116**:393–400.
27. Nackenhorst U. Numerical simulations of stress stimulated bone remodeling. *Technische Mechanik* 1997; **17**: 31–40.
28. Kuhl E, Menzel A, Steinmann P. Computational modeling of growth: a critical review, a classification of concepts and two new consistent approaches. *Computational Mechanics*, in press.
29. Carter DR, Hayes WC. The behavior of bone as a two-phase porous structure. *Journal of Bone and Joint Surgery* 1977; **59**(A):785–794.
30. Gibson LJ, Ashby MF. The mechanics of three-dimensional cellular materials. *Proceedings of the Royal Society of London* 1982; **A 382**:43–59.
31. Aifantis EC. On the microstructural origin of certain inelastic models. *Journal of Engineering Materials and Technology (ASME)* 1984; **106**:326–330.
32. Weng S. *Ein Evolutionsmodell zur mechanischen Analyse biologischer Strukturen*. Dissertation, Mitteilungen aus dem Institut für Mechanik, Ruhr-Universität Bochum, 1997.
33. Maute K. *Topologie- und Formoptimierung von dünnwandigen Tragwerken*. Dissertation, Bericht des Instituts für Baustatik Nr. 25, Universität Stuttgart, 1998.
34. Galileo G. *Discorsi e Dimostrazioni Matematiche Intorno a Due Nuove Scienze*. Appresso gli Elsevirii, Leida, 1638.
35. Kuhl E, Steinmann P. Geometrically nonlinear functional adaption of biological microstructures. In *WCCM V, Fifth World Congress on Computational Mechanics*, Mang HA, Rammerstorfer FG, Eberhardsteiner J (eds), <http://wccm.tuwien.ac.at>, 2002; Paper-ID: 80370.